ACS Catalysis

Research Article

Cite This: ACS Catal. 2019, 9, 3783−3791

pubs.acs.org/acscatalysis

Boosting CO Production in Electrocatalytic CO_2 Reduction on Highly Porous Zn Catalysts

Wen Luo,*[,†,‡] Jie Zhang,[†,‡] Mo Li,[†,‡] and Andreas Züttel[†,‡]

[†]Laboratory of Materials for Renewable Energy (LMER), Institute of Chemical Sciences and Engineering (ISIC), Basic Science Faculty (SB), École Polytechnique Fédérale de Lausanne (EPFL) Valais/Wallis, Energypolis, Rue de l'Industrie 17, CH-1951 Sion, Switzerland

[‡]Empa Materials Science & Technology, CH-8600 Dübendorf, Switzerland

Supporting Information

ABSTRACT: Earth-abundant electrocatalysts are desirable for the efficient and selective reduction of CO_2 to value-added chemicals. Here, a low-cost porous Zn electrocatalyst is synthesized using a facile electrodeposition method to boost the performance of CO_2 electrocatalytic reaction (CO_2RR). In an H-cell reactor, the porous Zn catalyst can convert CO_2 to CO at a remarkably high faradaic efficiency (FE, ~95%) and current density (27 mA cm^{-2}) at −0.95 V versus the reversible hydrogen electrode. Detailed electrokinetic studies demonstrate that instead of the enhanced intrinsic activity, the dramatically increased active sites play a decisive role in improving the catalytic activity. In addition, the high local pH induced by the highly porous structure of Zn results in enhanced CO selectivity because of the suppressed H_2 evolution. Furthermore, we present a straightforward strategy to transform the porous Zn electrode into a gas diffusion electrode. This way, the CO_2RR current density can be boosted to 200 mA cm^{-2} with ~84% FE for CO at −0.64 V in a flow-cell reactor, which is, to date, the best performance observed over non-noble CO_2RR catalysts.

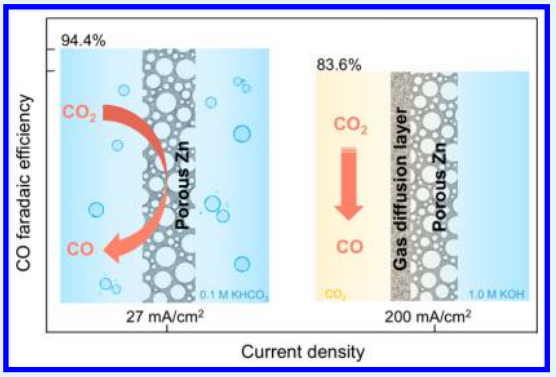

KEYWORDS: *CO_2 electrochemical reduction, Zn catalyst, catalytic mechanism, local pH effect, gas diffusion electrode*

1. INTRODUCTION

The electrocatalytic reduction of CO_2 (CO_2RR), powered by renewable electricity, is a promising strategy to mitigate high CO_2 levels in the atmosphere and to store the intermittent and low-energy-density renewable energy in the form of high-energy-density carbonaceous fuels.[1,2] A key challenge for the practical application of CO_2RR is the development of advanced catalysts. Even though various materials have been identified as being capable of reducing CO_2 in aqueous electrolytes, the reaction still suffers from low activity and product selectivity. The activity is limited by inefficient catalysts and the low concentration of CO_2 in neutral pH electrolytes (e.g., 0.1 M $KHCO_3$). The poor product selectivity is the result of a variety of proton-coupled multiple-electron transfer (PCET) processes, accompanied by the competitive hydrogen evolution reaction (HER). Therefore, great efforts have to be devoted to design advanced CO_2RR catalysts that can efficiently reduce CO_2 to the desired product at high selectivity.

Among various CO_2RR products, carbon monoxide (CO) is an important industrial raw chemical for processes such as the Fischer−Tropsch synthesis, methanol production, and pharmaceuticals' manufacture.[3,4] While noble metals, such as Au and Ag, have been recognized as the most efficient catalysts for reducing CO_2 to CO, their low abundance and high cost hinder the large-scale applications.[5−7] Zn, as an earth-abundant metal, can also reduce CO_2 to CO but with relative lower activity and CO selectivity than the Au and Ag catalysts.[8] To overcome these limitations, efforts have been made to synthesize nanostructured-Zn catalysts.[9−11] Various strategies, including electrodeposition,[12,13] anodization,[14] and oxide reduction,[13] have been employed. The obtained nanostructured-Zn electrodes often exhibit higher catalytic activity and CO selectivity compared with the bulk Zn electrodes. For example, hexagonal and dendritic Zn electrodes showed more than 9 and 2 times, respectively, higher total current densities in CO_2RR compared with those of the Zn foil electrodes.[12,15] In addition, some of the nanostructured-Zn electrodes also achieved ~90% faradaic efficiencies (FEs) for CO.[12,16,17]

While the nanostructured-Zn catalysts have shown enhanced CO_2RR performance, the key factors that influence the catalytic activity and selectivity were not clearly identified. For instance, even though comparisons have been made on the geometric current densities of nanostructured-Zn and bulk-Zn electrodes, the origin of the improved CO_2RR activity on nanostructured-Zn was not always unequivocally demonstrated

Received: December 23, 2018
Revised: February 24, 2019
Published: March 18, 2019

DOI: 10.1021/acscatal.8b05109
ACS Catal. 2019, 9, 3783−3791

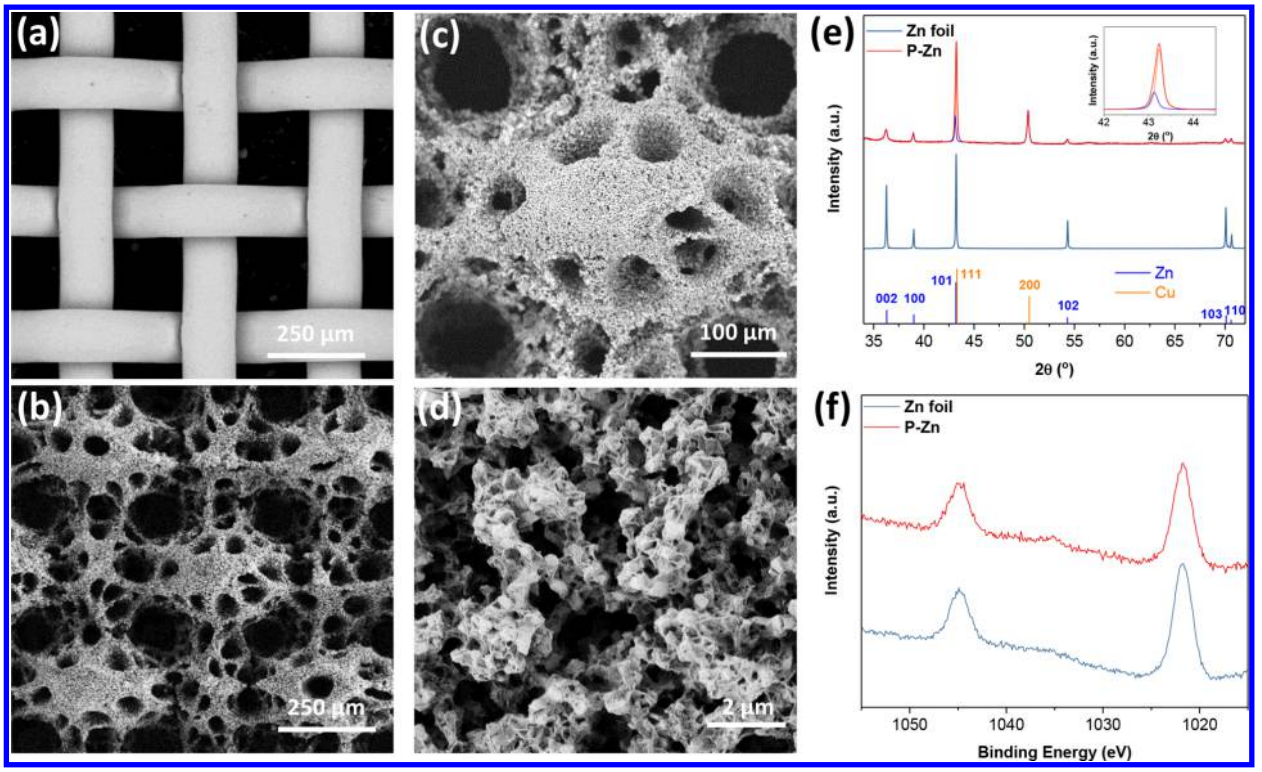

Figure 1. SEM image of (a) Cu mesh and (b)−(d) P−Zn. (e) XRD patterns of Zn foil and P−Zn. (f) XPS Zn 2p spectra for as-prepared P−Zn and Zn foil samples. The overlapped Zn(101) and Cu(111) peak for the P−Zn sample was deconvoluted and shown in the inset of (e).

because both the enhancement of intrinsic activity and enlargement of the surface area could promote the catalytic activity. Considering the improved CO selectivity, not only controversial active sites, including low-coordinated sites,[11,18] Zn(101) facet,[12,13,19] and grain boundaries,[17] were proposed as CO production centers but also external factors, such as the local electrolyte environment and mass transportation, were often overlooked.[20] Thus, the identification of the key variables that influence the performance of CO_2RR over nanostructured-Zn catalysts is essential for the rational design of advanced Zn-based catalysts and the optimization of reaction systems.

Concerning productivity, most of the Zn-based catalysts were evaluated in batch reactors (i.e., H-cell), where the current densities were limited to ∼10 mA cm^{-2} under reasonable overpotentials by the slow CO_2 mass transport.[9,19,21] In contrast, practical electrolysis cells typically operate in the >100 mA cm^{-2} regime. A flow-cell reactor, which separates the gas and liquid supply by a gas diffusion electrode (GDE), can overcome mass-transport limitations and thus allow a much higher CO_2RR current density. Nevertheless, previously reported Zn-based catalysts have not been, or cannot be, engineered to GDEs to test their performance under a high current density condition. Therefore, advanced Zn-based catalysts that are capable of being designed as GDEs and reducing CO_2 to CO at high current densities should be developed, in an effort to ultimately implement CO_2RR in large-scale applications.

Here we report a facile electrodeposition method to prepare highly active, selective, and stable porous-structured-Zn (P−Zn) electrodes for electrochemical reduction of CO_2 to CO. Through the simple deposition of Zn onto the Cu mesh substrate at a high current density, the obtained P−Zn electrode enables superior activity and CO selectivity in CO_2-saturated 0.1 M $KHCO_3$ electrolyte, which outcompetes the reported nanostructured-Zn catalysts under identical conditions. Moreover, with detailed electrokinetic investigation, we attribute the enhanced CO_2 reduction performance of the P−Zn electrode to the enlarged surface area and the strengthened local pH effect. In addition, we further boosted the current density to 200 mA cm^{-2} with ∼84% FE for CO by transforming the P−Zn electrode to a GDE used in a flow-cell reactor. Thus, we believe that the electrode-designing strategies and reaction-mechanism insights demonstrated in this work can inspire the development of other nanostructured catalysts for CO_2RR applications.

2. EXPERIMENTAL PART

Sample Preparation. P−Zn was electrodeposited on a piece of Cu mesh (80 mesh, Alfa Asear), using an aqueous solution of 1.5 M $(NH_4)_2SO_4$ (99.5%, Carl Roth) and 0.1 M $ZnSO_4{\cdot}7H_2O$ (99%−103%, Alfa Aesar). The electrodeposition was performed at a geometric current density of −1.0 mA cm^{-2} for 30 s. The average loading of Zn was 6.5 mg cm^{-2} (Table S1), measured using a high-precision microbalance (Mettler Toledo, d = 0.01 mg). A Zn foil (99.98%, Alfa Aesar) electrode was prepared by mechanically polishing (sandpaper, 3M) and cleaned by sonication in Milli-Q water.

For P−Zn-based GDEs, Zn was deposited on a Cu mesh (100 mesh, Alfa Asear) at −0.25 mA cm^{-2} for 60 s using the same solution as that for P−Zn. After washing and drying, the sample was immersed into PTFE dispersion (10 wt %, Sigma-Aldrich) for a few seconds to adsorb PTFE into the pores. Afterward, PTFE mixed with carbon black (Vulcan XC-72) dispersion (1:1) was sprayed onto one side of the sample to cover the pores and to form a hydrophobic layer. Finally, the sample was heated at 350 °C in N_2 for 30 min.

DOI: 10.1021/acscatal.8b05109
ACS Catal. 2019, 9, 3783−3791

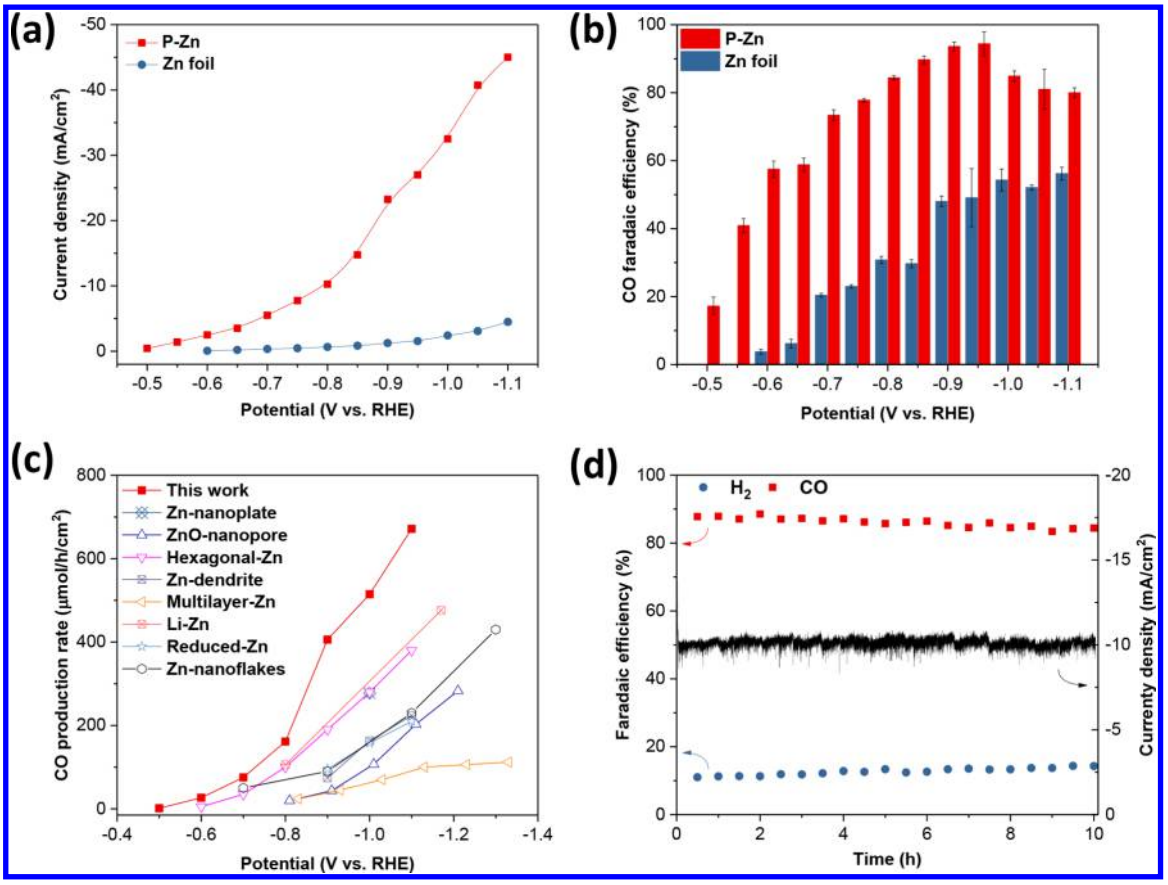

Figure 2. CO_2RR performance of P−Zn and Zn foil. Potential-dependent current density (a) and CO faradaic efficiency (b) for P−Zn and Zn foil. (c) Comparison of CO production rate observed over P−Zn and other state-of-the-art nanostructured Zn catalysts.[10−14,16,17,26] (d) Catalytic stability for P−Zn.

Materials Characterization. The scanning electron microscopy (SEM) analysis was performed on an FEI Teneo system. The X-ray diffraction (XRD) measurement was performed on a Bruker D8 Advance system using Cu Kα (λ = 1.54 Å) radiation. Transmission electron microscopy (TEM) images were taken on an FEI Tecnai G2 Spirit Twin system. The X-ray photoelectron spectroscopy (XPS) spectra were collected on a SPECS Phoibos 100 spectrometer using Mg Kα X-ray (hv = 1253.6 eV) source.

Electrochemical Measurements. All electrochemical measurements were performed with an Autolab potentiostat (PGSTAT 204 or PGSTAT302N), an Ag/AgCl (3 M NaCl, ALS) reference electrode, and a Pt foil counter electrode. All potentials were converted into reversible hydrogen electrode (RHE) through E (vs RHE) = E (vs Ag/AgCl) + 0.21 V + 0.0591 V × pH. The iR drop was compensated via the current interrupt method using 85% of the measured Ru.

The CO_2RR performance of Zn foil and P−Zn was evaluated in a conventional two-compartment H-cell reactor, using CO_2-saturated 0.1 M $KHCO_3$ (99.5%, Carl Roth) as electrolyte.[22,23] The cathodic and anodic compartments were separated with Nafion membrane (212, Dupont). The cathodic compartment was purged during the reaction with CO_2 (99.999%, Cabagas) at a constant rate of 21 mL min^{-1}.

The P−Zn-based GDEs were evaluated in a flow-cell reactor, which consists of a gas diffusion chamber, a cathodic counterpart and an anodic counterpart. CO_2 was introduced to the gas diffusion chamber at 40 mL min^{-1}. 1.0 M $KHCO_3$ or 1.0 M KOH (98%, Alfa Asear) electrolyte (10 mL) was circulated (at 10 mL min^{-1}) using a peristaltic pump through the cathodic counterpart, and another 10 mL of electrolyte was circulated through the anodic counterpart.

Gas and liquid products were quantified using gas chromatograph (GC, SRI instruments 8610C) and ^{1}H nuclear magnetic resonance spectroscopy (Bruker 400 MHz AVIII HD), respectively (details in Supporting Information).

3. RESULTS AND DISCUSSION

Catalyst Characterizations. The P−Zn electrode was prepared by the electrodeposition of Zn^{2+} onto a copper mesh at −1.0 A cm^{-2} for 30 s. Cu mesh, as a conductive support, enables the transportation of the electrolyte around the cathode and, therefore, ensures uniform growth of the deposited Zn. As confirmed by the SEM images shown in Figure 1b−d, P−Zn was homogeneously deposited on the Cu mesh support. The highly ordered macropores (Figure 1b) with diameters of ∼80 μm were inherited from the Cu mesh (Figure 1a), while the medium-sized pores (∼30 μm, Figure 1c) and small pores (<2 μm, Figure 1d) were generated during electrodeposition due to the simultaneous formation of hydrogen bubbles. Moreover, uniform porous Zn can also be deposited onto other supporting materials (e.g., Cu foil, Cu foam, and Ni mesh) (Figure S1), indicating the versatility of this method. The detailed morphology of P−Zn was investigated using TEM (Figure S2), where no oriented growth of Zn can be observed. The XRD results show that the crystal structure of P−Zn matches pure-metallic Zn (Figure 1e) except for two additional peaks at 2θ = 43.3° and 50.4°,

DOI: 10.1021/acscatal.8b05109
ACS Catal. 2019, 9, 3783−3791

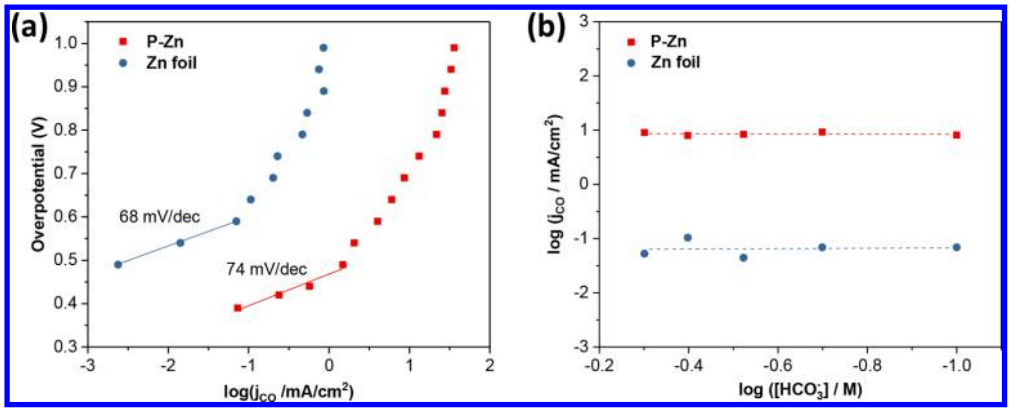

Figure 3. (a) Tafel plots for CO_2-to-CO over P−Zn and Zn foil in CO_2-saturated 0.1 M $KHCO_3$ electrolyte. (b) Bicarbonate ion concentration dependence of CO partial current density at −0.7 V for P−Zn and Zn foil in CO_2-saturated $KHCO_3$ electrolytes (KCl was added to keep the total K^+ concentration at 0.5 M).

which are attributed to the Cu mesh support. Different from the XRD results, the spectra of Cu were not observed in the XPS survey scan (Figure S3), indicating that the Zn deposit fully covered the surface of Cu mesh. Figure 1f shows the Zn 2p XPS spectrum of P−Zn, with Zn $2p_{3/2}$ at 1021.7 eV and Zn $2p_{1/2}$ at 1044.7 eV. While it is difficult to distinguish Zn and ZnO from XPS spectra because of their similar binding energy values, the identical peak shape, full width at half-maximum as well as the peak position of P−Zn and Zn foil are indicative of their identical surface chemical state.[24,25]

Electrocatalytic Reduction of CO_2. The electrocatalytic performance of Zn foil and P−Zn was first evaluated in CO_2- or He-purged 0.1 M $KHCO_3$ electrolyte in H-cell reactor. Linear sweep voltammetry (LSV) results (Figure S4) show that both the Zn foil and P−Zn samples exhibit higher current densities in CO_2-saturated electrolyte than those obtained in He-saturated electrolyte, indicating that the Zn electrodes are active toward CO_2 reduction. In addition, the P−Zn sample exhibits much higher current densities compared with the Zn foil sample, which could be attributed to its enlarged surface area.

To get a better understanding on the CO_2RR activity as well as the product distribution, potentiostatic CO_2 electrolysis was performed in the potential range of −0.5 V to −1.1 V on the Zn foil and P−Zn electrodes. In accordance with the LSV results, the total current densities obtained at constant potentials confirm the higher activity of P−Zn than Zn foil (Figure 2a), where the values for P−Zn are about 15 times as high as those for Zn foil at the studied potentials. The main product from CO_2 electrolysis is CO, accompanied by a small amount of formate detected at high overpotentials (Figure S5). As a byproduct from the H_2O reduction, H_2 was also detected in the entire potential range.[11,16] Figure 2b shows the potential-dependent FEs for CO on the Zn foil and P−Zn electrodes. It is clear that the FEs for CO are systematically higher on P−Zn than on Zn foil in the measured potential range, and the difference mainly corresponds to lower FEs for H_2 on P−Zn (Figure S5). In addition, the CO FE for the Zn foil electrode increases with the increase of overpotential and reaches maximum values of ∼55% at potentials below −1.0 V. In contrast, the CO FE for P−Zn is already higher than 55% at −0.6 V, which is a positive shift of 400 mV compared with that of Zn foil. More importantly, the FE for CO reaches 94.4% at −0.95 V on P−Zn, which is significantly higher than that for Zn foil and represents the highest CO_2-to-CO selectivity among the reported Zn electrodes at the same overpotential (Table S2). Further decreasing of the applied potential leads to a decrease of CO FE on P−Zn, which could be attributed to the mass-transport limitations for CO_2RR at high current densities. Because of the high current density and CO selectivity, the CO production rates on P−Zn surpass those of previously reported Zn catalysts in a wide potential range. In particular, at −1.1 V, the CO production rate reaches an unprecedented value of 671 μmol h^{-1} cm^{-2}. In addition to P−Zn, we also performed control experiments over blank Cu mesh and porous Zn supported on Ni mesh (Figure S6). In the entire potential range, the blank Cu mesh shows 1 order of magnitude lower CO production rate than that of P−Zn, however, the Ni mesh-supported porous Zn exhibits similar CO_2RR performance as P−Zn. Since bulk Ni is known to be inert for CO_2RR, these results demonstrate that the high current density and CO selectivity are attributed to the porous-Zn deposit rather than the mesh supports.

To evaluate the long-term performance of the P−Zn electrode, electrolysis at −0.8 V was carried out over an extended period. As shown in Figure 2d, the current density is stable at ∼10 mA cm^{-2} and the FE for CO remains essentially unchanged (∼85%) over 10 h, suggesting a high durability of P−Zn for CO_2RR. The SEM results of the sample after the stability test (Figure S7) revealed that P−Zn well preserved its 3D porous structure.

Origin of the Superior CO_2RR Performance over P−Zn. To elucidate the origin of the improved CO_2RR performance over the P−Zn electrode, we performed detailed electrokinetic studies to compare the CO_2 reduction pathways on both Zn foil and P−Zn catalysts. Based on the previously proposed CO_2-to-CO mechanisms,[27,28] four elementary reaction steps can be suggested as

$$*CO_2 + e^- \rightarrow *CO_2^- \quad (1)$$

$$*CO_2^- + H^+(aq) \rightarrow *COOH \quad (2)$$

$$*COOH + H^+(aq) + e^- \rightarrow *CO + H_2O(l) \quad (3)$$

$$*CO \rightarrow CO(g) + * \quad (4)$$

where * refers as an active site. While it is clear that the reduction of CO_2 to CO involves two electrons and two protons, the rate-determining step (RDS) of this reaction seems strongly influenced by the nature of the catalyst (e.g.,

DOI: 10.1021/acscatal.8b05109
ACS Catal. 2019, 9, 3783−3791

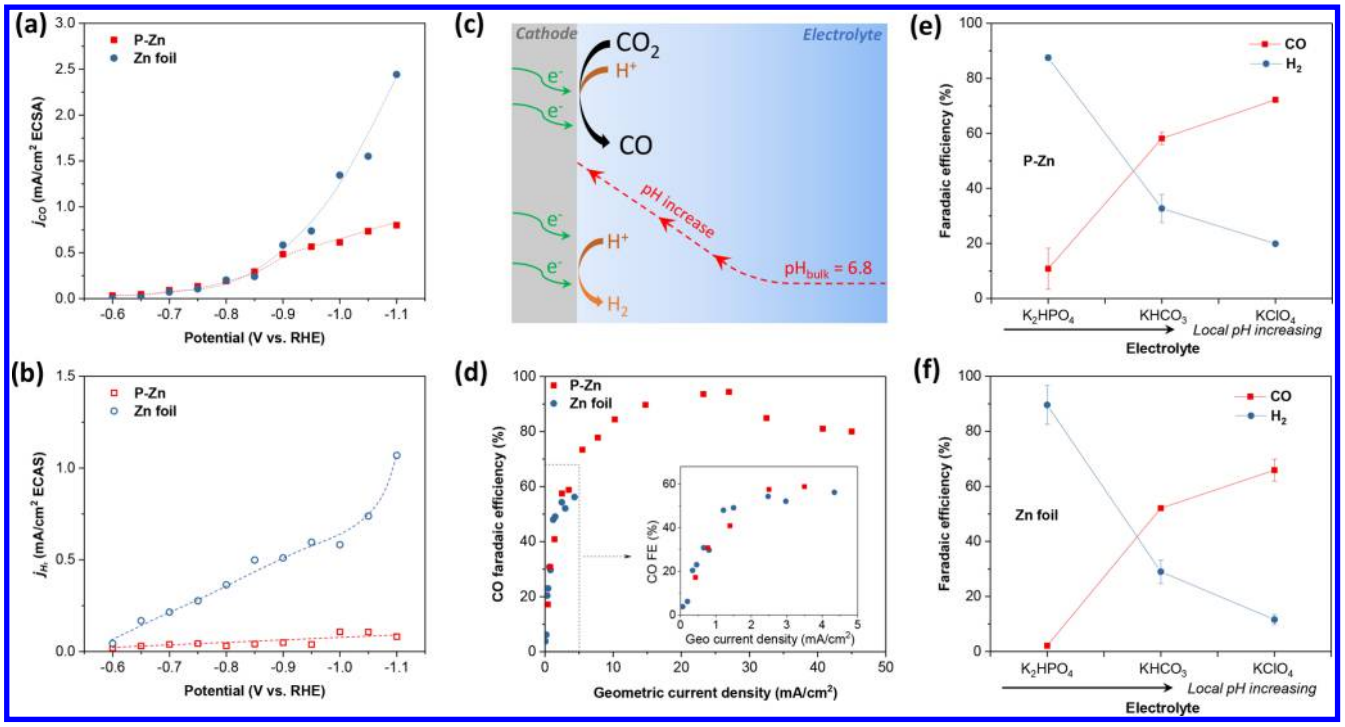

Figure 4. ECSA-normalized (a) CO and (b) H_2 partial current densities for P−Zn and Zn foil catalysts; the dashed lines are drawn as a guide to the eye. (c) Schematic illustration of local pH effect in CO_2RR. (d) Faradaic efficiency of CO as a function of geometric current density observed over P−Zn and Zn foil catalysts. Faradaic efficiency for CO and H_2 measured at 3.0 mA cm^{-2} in CO_2-saturated 0.1 M K_2HPO_4, 0.1 M $KHCO_3$, and 0.1 M $KClO_4$ for (e) P−Zn and (f) Zn foil.

the type of metal, surface oxidation state, and crystal structure).[27−29] To determine the RDS of CO_2RR on our Zn catalysts, Tafel analysis was performed. By comparing the experimentally observed Tafel slopes (logarithm of the partial current density toward a specific product versus overpotential) with the theoretical calculated slopes (obtained on the basis of a proposed mechanism and RDS), it is possible to suggest the reaction pathways and the RDS.[30] As shown in Figure 3a, the Tafel slopes measured on Zn foil and P−Zn are 68 and 74 mV dec^{-1}, respectively, which are close to the theoretical value of 59 mV dec^{-1} for a rate-limiting chemical step.[30] This indicates that the initial electron transfer (ET) step (eq 1) is not the RDS, but the proton transfer (PT) step (eq 2) is more plausible as the RDS for both Zn catalysts. This result is quite intriguing because the Tafel slopes of bulk-Zn electrodes were previously reported to be higher than 100 mV dec^{-1}, and the RDS of CO_2RR on bulk Zn was therefore suggested as the initial ET step. Indeed, those high slopes were generally obtained at relatively high overpotentials (>0.6 V) because the low-surface-area bulk-Zn electrodes require high overpotentials to enable sufficient CO production rates for Tafel plots.[11,16,18] However, the Tafel slope is strongly influenced by the mass transport and the coverage of intermediates on the electrode surface.[30] Therefore, we propose that the high Tafel slopes of near 118 mV dec^{-1}, observed previously for bulk-Zn electrodes, may not be strictly determined by electrokinetics but overestimated because of the mass-transport limitations. Taken together, we suggest that the CO_2RR on both Zn foil and P−Zn electrodes follows the same reaction pathway, which is a fast ET step followed by a rate-limiting PT step and a final PCET step. In addition, these results also highlight the importance of performing the Tafel analysis at low overpotentials where the reaction is only controlled by electrokinetics.[30]

As the reaction rates on both types of Zn catalysts are limited by the PT step, we sought to understand the influence of proton donor environment on the CO_2RR activity. Previously, HCO_3^- has been assumed as the proton donor in the initial PT step, since an approximately first-order dependence of CO production rate on the HCO_3^- concentration has been observed.[31] By performing the electrolysis of CO_2 in $KHCO_3$ electrolytes with different concentrations (0.1 to 0.5 M), however, we found that the rates of CO production on both electrodes are insensitive to the HCO_3^- concentration (Figure 3b). This indicates that the donation of a proton from H_2O or H_3O^+, rather than HCO_3^- should be the RDS for CO_2RR on both Zn electrodes.[29,32] HCO_3^-, on the other hand, may serve as a reservoir for the reactants CO_2 and H^+.[33]

Since both of the Zn catalysts follow identical CO_2-to-CO mechanisms, it is essential to explore other variables that influence the performance of Zn foil and P−Zn electrodes. As the activity improvement of a nanostructured-electrocatalyst may originate from the enhanced intrinsic activity and/or the increased number of active sites,[34] to deconvolute these two factors we compared the intrinsic activity of the two Zn catalysts by normalizing the $j_{(CO)}$ to the electrochemical surface area (ECSA), which was estimated from the capacitance measurements (Figure S8). As shown in Figure 4a, both catalysts display identical ECSA-normalized $j_{(CO)}$ at low overpotentials. Indeed, by plotting the ECSA-normalized $j_{(CO)}$ of other previously reported Zn-based catalysts (Figure S9), we found that state-of-the-art nanostructured-Zn catalysts also exhibit similar intrinsic activities to those of the bulk Zn catalysts.[9−11,16,26] Thus, it is reasonable to conclude that the

DOI: 10.1021/acscatal.8b05109
ACS Catal. 2019, 9, 3783−3791

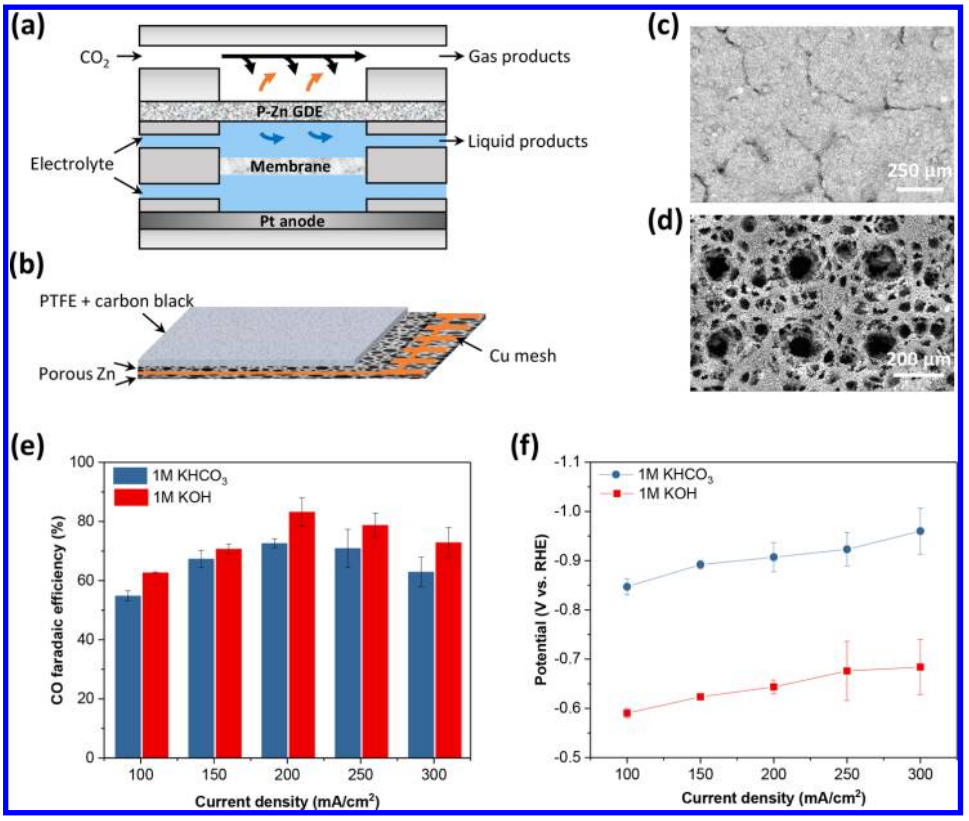

Figure 5. Schematic illustration of (a) flow-cell reactor and (b) P−Zn based GDE. SEM images of P−Zn-based GDE for (c) gas diffusion side (PTFE + carbon black) and (d) electrolyte side (porous Zn). (e) CO faradaic efficiency and (f) the applied potential as a function of geometric current density obtained in 1.0 M $KHCO_3$ and 1.0 M KOH electrolytes.

activity difference between the nanostructured-Zn and the planar-Zn catalysts is mainly due to the increased number of active sites rather than the enhanced intrinsic activity. Notably, at higher overpotentials, the ECSA-normalized $j_{(CO)}$ of P−Zn is lower than that of Zn foil because mass transfer is limiting the supply of CO_2 to the P−Zn surface.[34] This implies that mitigating the effects of mass transfer through different strategies, such as increasing the forced convection of CO_2 in the electrolyte and using a flow-cell reactor, is possible to further improve the performance of the P−Zn catalyst.

While both the P−Zn and Zn foil catalysts exhibit comparable intrinsic activities for CO_2-to-CO, the reduced H_2 evolution rate over P−Zn, as shown in Figure 4b, leads to the improved CO selectivity. We propose that the suppressed HER activity over P−Zn is a result of the local pH effect.[8,28] As illustrated in Figure 4c, since CO_2RR was performed in an electrolyte with weak buffer capacity (i.e., CO_2/HCO_3^-), the proton consumption in cathodic reactions (CO_2RR and HER) would lead to the rise of pH near the electrode.[8,28,35] Under the same applied potential, P−Zn exhibits much higher geometric current density than that of Zn foil (Figure 2a), which would lead to a more significant local pH effect and therefore a more effective suppression of HER activity.[8,28] To test this hypothesis, we plotted the FEs of CO for P−Zn and Zn foil against the geometric current density instead of the applied potential. As shown in Figure 4d, the P−Zn and Zn foil catalysts display similar CO FEs slopes. This suggests that, under the same current density, and therefore a similar local pH environment, the two electrodes exhibit comparable CO selectivity. In addition, through varying the electrodeposition time for preparing porous Zn samples, we also obtained a series of porous Zn electrodes with different Zn loading and surface area (Figure S10). Although those catalysts show different activity and CO FE at a constant potential, their CO selectivity, when plotted against the current density, is similar to that of Zn foil and P−Zn. These results demonstrate that the increased surface area of porous Zn catalysts leads to a high current density and local pH, thereby suppressing the H_2 evolution rate.

To further verify the local pH effect, we evaluated the Zn foil and P−Zn samples in CO_2-saturated 0.1 M K_2PO_4, 0.1 M $KHCO_3$, and 0.1 M $KClO_4$ electrolyte at a constant current condition (3.0 mA cm^{-2}). Because of the different buffer abilities of these three electrolytes (i.e., 0.1 M K_2HPO_4 > 0.1 M $KHCO_3$ > 0.1 M $KClO_4$), the locally increased OH^- concentration will be mitigated to different extents; the local pH is then expected in the order K_2HPO_4 < $KHCO_3$ < $KClO_4$. Figure 4e,f shows the FEs for CO and H_2 of the P−Zn and Zn foil catalysts in different electrolytes. For both electrodes, the FEs for H_2 are dramatically reduced as the local pH increases, and therefore, the FEs for CO are significantly improved. This confirms that a high local pH is preferred for CO_2RR rather than HER. In addition, comparing the results obtained in the same electrolyte for P−Zn and Zn foil, we find that the two electrodes show comparable selectivity. This agrees well with the above finding that the two electrodes exhibit similar intrinsic activity. Showing here the dramatic influence of local pH on the reaction selectivity, we emphasize the importance of considering the effects of local pH in interpreting the enhanced CO_2RR selectivity over nanostructured catalysts. This is particularly important when comparisons are made between planar and nanostructured catalysts, as is often the case,

DOI: 10.1021/acscatal.8b05109
ACS Catal. 2019, 9, 3783−3791

because the greatly disparate surface areas can vary the local pH environment dramatically. Taken together, we can conclude that the superior CO_2RR performance over the P−Zn catalyst primarily originates from its high surface area, which improves the catalytic activity and selectivity by increasing the number of active sites and enhancing the local pH effect, respectively.

Performance of P−Zn as a GDE in a Flow-Cell Reactor. Evaluation of CO_2RR catalysts in an H-cell reactor is an effective means for screening catalysts, understanding structure−performance relationships, and gaining mechanism insights. However, in a typical H-cell, the maximum geometric current density is limited to the order of 10 mA cm^{-2} by the low solubility of CO_2 in aqueous solutions (~33.4 mM). Moreover, despite that high local pH being preferred for CO_2RR over HER, alkaline electrolytes cannot be used in H-cell reactors because dissolved CO_2 only exists in neutral and low pH electrolytes.[36] To overcome these limitations, a GDE can be designed to work in a flow-cell system, where gas and liquid are separated and thus the solution phase mass-transport constraint is removed (Figure 5a).[37] Conventional GDEs are prepared by the deposition of catalysts onto the gas diffusion layer (e.g., carbon paper),[38−41] which limits the application of catalysts that are grown on substrates, including some oxide-derived metals,[42,43] nanostructured metals,[9] and bimetallic catalysts.[22,44] Here, we present a new strategy to design GDEs based on the porous structure of the catalyst (Figure 5b−d). To fabricate P−Zn-based GDE, we first immersed the P−Zn electrode into PTFE dispersion to coat with a layer of PTFE, which provides hydrophobic pores as the gas−liquid−solid interface. A layer of carbon black and PTFE mixture was then sprayed onto the gas diffusion side of the GDE to cover the pores and thus prevent the electrolyte from penetrating the GDE (Figure 5c). Finally the GDE was annealed under N_2 atmosphere to soften the PTFE and improve the hydrophobicity. With this strategy, other nanostructured catalysts can also be grown on a mesh or porous substrate and then engineered to a GDE, which allows the evaluation and application of those catalysts at high current density conditions.

The performance of the as-prepared P−Zn-based GDE was first evaluated in 1.0 M $KHCO_3$ electrolyte in the flow-cell reactor (Figure 5a). As shown in Figure 5e,f, the current density for CO_2RR can be significantly improved in the flow-cell configuration, with 300 mA cm^{-2} achieved at −0.95 V. Similar as in H-cell, only CO and H_2 were detected as major reduction products with trace amount of formate detected as the liquid product (Figure S11). Figure 5e shows that the FE for CO increases with the applied current density and reaches to a peak value of ~73% at 200 mA cm^{-2}. At higher applied current densities, the CO selectivity declines, possibly due to the high-rate gas evolution that limits the access of CO_2 to the electrode.[45]

We then sought to further improve the CO_2RR performance of P−Zn-based GDE in alkaline media (1.0 M KOH), in which it has been reported that the reaction overpotential and selectivity for CO_2RR can be improved.[21,36] As shown in Figure 5f, the overpotential required for achieving the same current density is decreased by ~250 mV in 1.0 M KOH compared with that of 1.0 M $KHCO_3$. Furthermore, at all the measured current densities, the FEs for CO were found to be improved by ~10% in 1.0 M KOH (Figure 5e). In particular, at a current density of 200 mA cm^{-2} and applied potential of −0.64 V, the highest FE for CO of ~84% was achieved. At more negative potential (−0.68 V), the total current density could be further boosted to 300 mA cm^{-2} with FE for CO of ~73%. Compared with the performance of other reported GDEs for CO_2-to-CO, the P−Zn catalyst represents the most efficient non-noble metal catalyst and is comparable with the state-of-the-art noble metal (e.g., Ag and Au) catalysts (Table S3).[21,40,46−49] Moreover, at a fixed potential of −0.55 V in 1.0 M KOH electrolyte, the P−Zn-based GDE also exhibited stable current density and CO FE for extended testing time of 6 h (Figure S12). These results demonstrate the great potential of P−Zn-based GDE for large-scale electroreduction of CO_2 to CO.

4. CONCLUSIONS

In summary, highly porous Zn-based electrodes were synthesized via a facile electrodeposition method for CO_2RR. In an H-cell configuration, the as-prepared catalyst exhibited a maximum CO FE of ~95% at −0.95 V and a CO production rate of 671 μmol h^{-1} cm^{-2} at −1.1 V, exceeding the performance of previously reported nanostructured-Zn catalysts. The comparison between P−Zn and Zn foil electrodes demonstrated that CO_2-to-CO follows identical reaction pathways on these two catalysts and the first proton transfer step is the RDS. The dramatically improved catalytic activity and selectivity for CO_2-to-CO are primarily attributed to the highly porous structure of P−Zn, which increases the number of active sites and strengthens the local pH effect. These results highlight the importance of detailed mechanism studies and analysis in interpreting the enhanced performance of nanostructured CO_2RR catalysts. In addition, we also provided a novel strategy to fabricate GDE directly based on the P−Zn electrode, which enables the current density to be boosted to 200 mA cm^{-2} with ~84% CO FE at −0.64 V. Thus, this work not only offers P−Zn as a high-performance CO_2RR catalyst but also provides new electrode design strategies and mechanistic insights to guide the development of other low-cost and active electrocatalysts toward large-scale CO_2RR applications.

■ ASSOCIATED CONTENT

Supporting Information

The Supporting Information is available free of charge on the ACS Publications website at DOI: 10.1021/acscatal.8b05109.

(Mass loading of Zn; SEM images of Zn with different loading and on other substrates; SEM images of P−Zn after stability test; TEM images of P−Zn; XPS survey scan; LSVs of P−Zn and Zn foil; ECSA results; products' distribution of Zn foil, P−Zn and P−Zn-based GDE; performance of P−Zn with different Zn loading and Cu mesh, and Ni mesh-supported porous Zn; performance comparison of Zn-based catalysts and various GDEs; comparison of ECSA-normalized CO current density of Zn-based catalysts PDF)

■ AUTHOR INFORMATION

Corresponding Author

*E-mail: wen.luo@epfl.ch.

ORCID

Wen Luo: 0000-0003-4250-6168

DOI: 10.1021/acscatal.8b05109
ACS Catal. 2019, 9, 3783−3791

Notes

The authors declare no competing financial interest.

■ ACKNOWLEDGMENTS

This research is supported by Swiss National Science Foundation (Ambizione Project PZ00P2_179989). This research is also part of the activities of SCCER HeE, which is financially supported by Innosuisse-Swiss Innovation Agency. M.L. acknowledges the Ph.D. scholarship from China Scholarship Council (Grant No. 201506060156).

■ REFERENCES

(1) Spurgeon, J. M.; Kumar, B. A Comparative Technoeconomic Analysis of Pathways for Commercial Electrochemical CO_2 Reduction to Liquid Products. *Energy Environ. Sci.* **2018**, *11*, 1536−1551.
(2) Lewis, N. S.; Nocera, D. G. Powering the Planet: Chemical Challenges in Solar Energy Utilization. *Proc. Natl. Acad. Sci. U. S. A.* **2006**, *103*, 15729−15735.
(3) Dry, M. E. The Fischer - Tropsch Process: 1950−2000. *Catal. Today* **2002**, *71*, 227−241.
(4) van de Loosdrecht, J.; Niemantsverdriet, J. W. Synthesis Gas to Hydrogen, Methanol, and Synthetic Fuels. *Chemical Energy Storage* **2012**, 443.
(5) Lu, Q.; Rosen, J.; Zhou, Y.; Hutchings, G. S.; Kimmel, Y. C.; Chen, J. G.; Jiao, F. A Selective and Efficient Electrocatalyst for Carbon Dioxide Reduction. *Nat. Commun.* **2014**, *5*, 3242.
(6) Liu, M.; Pang, Y.; Zhang, B.; De Luna, P.; Voznyy, O.; Xu, J.; Zheng, X.; Dinh, C. T.; Fan, F.; Cao, C.; Garcia de Arquer, F. P.; Safaei, T. S.; Mepham, A.; Klinkova, A.; Kumacheva, E.; Filleter, T.; Sinton, D.; Kelley, S. O.; Sargent, E. H. Enhanced Electrocatalytic CO_2 Reduction via Field-Induced Reagent Concentration. *Nature* **2016**, *537*, 382−386.
(7) Song, J. T.; Ryoo, H.; Cho, M.; Kim, J.; Kim, J. G.; Chung, S. Y.; Oh, J. Nanoporous Au Thin Films on Si Photoelectrodes for Selective and Efficient Photoelectrochemical CO_2 Reduction. *Adv. Energy Mater.* **2017**, *7*, 1601103.
(8) Hori, Y. Electrochemical CO_2 Reduction on Metal Electrodes. *Mod. Asp. Electrochem.* **2008**, *42*, 89−189.
(9) Won, D. H.; Shin, H.; Koh, J.; Chung, J.; Lee, H. S.; Kim, H.; Woo, S. I. Highly Efficient, Selective, and Stable CO_2 Electroreduction on a Hexagonal Zn Catalyst. *Angew. Chem., Int. Ed.* **2016**, *55*, 9297−9300.
(10) Jiang, X.; Cai, F.; Gao, D.; Dong, J.; Miao, S.; Wang, G.; Bao, X. Electrocatalytic Reduction of Carbon Dioxide over Reduced Nanoporous Zinc Oxide. *Electrochem. Commun.* **2016**, *68*, 67−70.
(11) Rosen, J.; Hutchings, G. S.; Lu, Q.; Forest, R. V.; Moore, A.; Jiao, F. Electrodeposited Zn Dendrites with Enhanced CO Selectivity for Electrocatalytic CO_2 Reduction. *ACS Catal.* **2015**, *5*, 4586−4591.
(12) Lee, H. S.; Chung, J.; Shin, H.; Kim, H.; Koh, J.; Woo, S. I.; Won, D. H. Highly Efficient, Selective, and Stable CO_2 Electroreduction on a Hexagonal Zn Catalyst. *Angew. Chem., Int. Ed.* **2016**, *55*, 9297−9300.
(13) Qin, B.; Li, Y.; Fu, H.; Wang, H.; Chen, S.; Liu, Z.; Peng, F. Electrochemical Reduction of CO_2 into Tunable Syngas Production by Regulating the Crystal Facets of Earth-Abundant Zn Catalyst. *ACS Appl. Mater. Interfaces* **2018**, *10*, 20530−20539.
(14) Quan, F.; Zhong, D.; Song, H.; Jia, F.; Zhang, L. A Highly Efficient Zinc Catalyst for Selective Electroreduction of Carbon Dioxide in Aqueous NaCl Solution. *J. Mater. Chem. A* **2015**, *3*, 16409−16413.
(15) Zhao, Z.; Lu, G. Computational Screening of Near-Surface Alloys for CO_2 Electroreduction. *ACS Catal.* **2018**, *8*, 3885−3894.
(16) Zhang, T.; Li, X.; Qiu, Y.; Su, P.; Xu, W.; Zhong, H.; Zhang, H. Multilayered Zn Nanosheets as an Electrocatalyst for Efficient Electrochemical Reduction of CO_2. *J. Catal.* **2018**, *357*, 154−162.
(17) Jiang, K.; Wang, H.; Cai, W.-B.; Wang, H. Li Electrochemical Tuning of Metal Oxide for Highly Selective CO_2 Reduction. *ACS Nano* **2017**, *11*, 6451−6458.
(18) Jiang, X.; Cai, F.; Gao, D.; Dong, J.; Miao, S.; Wang, G.; Bao, X. Electrocatalytic Reduction of Carbon Dioxide over Reduced Nanoporous Zinc Oxide. *Electrochem. Commun.* **2016**, *68*, 67−70.
(19) Moreno-García, P.; Schlegel, N.; Zanetti, A.; Cedeño Lopez, A.; Gálvez-Vazquez, M. d. J.; Dutta, A.; Rahaman, M.; Broekmann, P. Selective Electrochemical Reduction of CO_2 to CO on Zn-Based Foams Produced by Cu^{2+} and Template-Assisted Electrodeposition. *ACS Appl. Mater. Interfaces* **2018**, *10*, 31355−31365.
(20) Kortlever, R.; Shen, J.; Schouten, K. J. P.; Calle-Vallejo, F.; Koper, M. T. M. Catalysts and Reaction Pathways for the Electrochemical Reduction of Carbon Dioxide. *J. Phys. Chem. Lett.* **2015**, *6*, 4073−4082.
(21) Dinh, C.-T.; Garcia de Arquer, F. P.; Sinton, D.; Sargent, E. H. High Rate, Selective and Stable Electroreduction of CO_2 to CO in Basic and Neutral Media. *ACS Energy Lett.* **2018**, *3*, 2835−2840.
(22) Luo, W.; Xie, W.; Mutschler, R.; Oveisi, E.; De Gregorio, G. L.; Buonsanti, R.; Zuttel, A. Selective and Stable Electroreduction of CO_2 to CO at the Copper/Indium Interface. *ACS Catal.* **2018**, *8*, 6571−6581.
(23) Xie, W.; Züttel, A.; Li, M.; Luo, W.; Zhang, J. 3D Hierarchical Porous Indium Catalyst for Highly Efficient Electroreduction of CO_2. *J. Mater. Chem. A* **2019**, *7*, 4505.
(24) Wöll, C. The Chemistry and Physics of Zinc Oxide Surfaces. *Prog. Surf. Sci.* **2007**, *82*, 55−120.
(25) Luo, W.; Baaziz, W.; Cao, Q.; Ba, H.; Baati, R.; Ersen, O.; Pham-Huu, C.; Zafeiratos, S. Design and Fabrication of Highly Reducible PtCo Particles Supported on Graphene-Coated ZnO. *ACS Appl. Mater. Interfaces* **2017**, *9*, 34256−34268.
(26) Nguyen, D. L. T.; Jee, M. S.; Won, D. H.; Jung, H.; Oh, H. S.; Min, B. K.; Hwang, Y. J. Selective CO_2 Reduction on Zinc Electrocatalyst: The Effect of Zinc Oxidation State Induced by Pretreatment Environment. *ACS Sustainable Chem. Eng.* **2017**, *5*, 11377−11386.
(27) Rosen, J.; Hutchings, G. S.; Lu, Q.; Rivera, S.; Zhou, Y.; Vlachos, D. G.; Jiao, F. Mechanistic Insights into the Electrochemical Reduction of CO_2 to CO on Nanostructured Ag Surfaces. *ACS Catal.* **2015**, *5*, 4293−4299.
(28) Ma, M.; Trzesniewski, B. J.; Xie, J.; Smith, W. A. Selective and Efficient Reduction of Carbon Dioxide to Carbon Monoxide on Oxide-Derived Nanostructured Silver Electrocatalysts. *Angew. Chem., Int. Ed.* **2016**, *55*, 9748−9752.
(29) Singh, M. R.; Goodpaster, J. D.; Weber, A. Z.; Head-Gordon, M.; Bell, A. T. Mechanistic Insights into Electrochemical Reduction of CO_2 over Ag Using Density Functional Theory and Transport Models. *Proc. Natl. Acad. Sci. U. S. A.* **2017**, *114*, E8812−E8821.
(30) Dunwell, M.; Luc, W. W.; Yan, Y.; Jiao, F.; Xu, B. Understanding Surface-Mediated Electrochemical Reactions: CO_2 Reduction and Beyond. *ACS Catal.* **2018**, *8*, 8121−8129.
(31) Ma, M.; Liu, K.; Shen, J.; Kas, R.; Smith, W. A. In Situ Fabrication and Reactivation of Highly Selective and Stable Ag Catalysts for Electrochemical CO_2 Conversion. *ACS Energy Lett.* **2018**, *3*, 1301−1306.
(32) Wuttig, A.; Yaguchi, M.; Motobayashi, K.; Osawa, M.; Surendranath, Y. Inhibited Proton Transfer Enhances Au-Catalyzed CO_2-to-Fuels Selectivity. *Proc. Natl. Acad. Sci. U. S. A.* **2016**, *113*, E4585−E4593.
(33) Hegner, R.; Rosa, L. F. M.; Harnisch, F. Electrochemical CO_2 Reduction to Formate at Indium Electrodes with High Efficiency and Selectivity in pH Neutral Electrolytes. *Appl. Catal., B* **2018**, *238*, 546−556.
(34) Clark, E. L.; Resasco, J.; Landers, A.; Lin, J.; Chung, L. T.; Walton, A.; Hahn, C.; Jaramillo, T. F.; Bell, A. T. Standards and Protocols for Data Acquisition and Reporting for Studies of the Electrochemical Reduction of Carbon Dioxide. *ACS Catal.* **2018**, *8*, 6560−6570.
(35) Ma, M.; Djanashvili, K.; Smith, W. A. Controllable Hydrocarbon Formation from the Electrochemical Reduction of CO_2 over Cu Nanowire Arrays. *Angew. Chem., Int. Ed.* **2016**, *55*, 6680−6684.

DOI: 10.1021/acscatal.8b05109
ACS Catal. 2019, 9, 3783−3791

(36) Kibria, M. G.; Dinh, C.-T.; Seifitokaldani, A.; De Luna, P.; Burdyny, T.; Quintero-Bermudez, R.; Ross, M. B.; Bushuyev, O. S.; García de Arquer, F. P.; Yang, P.; Sinton, D.; Sargent, E. H. A Surface Reconstruction Route to High Productivity and Selectivity in CO_2 Electroreduction toward C_{2+} Hydrocarbons. *Adv. Mater.* **2018**, *30*, 1804867.
(37) Ma, S.; Sadakiyo, M.; Luo, R.; Heima, M.; Yamauchi, M.; Kenis, P. J. A. One-Step Electrosynthesis of Ethylene and Ethanol from CO_2 in an Alkaline Electrolyzer. *J. Power Sources* **2016**, *301*, 219−228.
(38) García de Arquer, F. P.; Bushuyev, O. S.; De Luna, P.; Dinh, C. T.; Seifitokaldani, A.; Saidaminov, M. I.; Tan, C. S.; Quan, L. N.; Proppe, A.; Kibria, M. G.; Kelley, S. O.; Sinton, D.; Sargent, E. H. 2D Metal Oxyhalide-Derived Catalysts for Efficient CO_2 Electroreduction. *Adv. Mater.* **2018**, *30*, 1802858.
(39) Zhuang, T. T.; Liang, Z. Q.; Seifitokaldani, A.; Li, Y.; De Luna, P.; Burdyny, T.; Che, F.; Meng, F.; Min, Y.; Quintero-Bermudez, R.; Dinh, C. T.; Pang, Y.; Zhong, M.; Zhang, B.; Li, J.; Chen, P. N.; Zheng, X. L.; Liang, H.; Ge, W. N.; Ye, B. J.; Sinton, D.; Yu, S. H.; Sargent, E. H. Steering Post-C-C Coupling Selectivity Enables High Efficiency Electroreduction of Carbon Dioxide to Multi-Carbon Alcohols. *Nat. Catal.* **2018**, *1*, 421−428.
(40) Hoang, T. T. H.; Verma, S.; Ma, S.; Fister, T. T.; Timoshenko, J.; Frenkel, A. I.; Kenis, P. J. A.; Gewirth, A. A. Nanoporous Copper-Silver Alloys by Additive-Controlled Electrodeposition for the Selective Electroreduction of CO_2 to Ethylene and Ethanol. *J. Am. Chem. Soc.* **2018**, *140*, 5791−5797.
(41) Hoang, T. T. H.; Ma, S.; Gold, J. I.; Kenis, P. J. A.; Gewirth, A. A. Nanoporous Copper Films by Additive-Controlled Electrodeposition: CO_2 Reduction Catalysis. *ACS Catal.* **2017**, *7*, 3313−3321.
(42) Li, C. W.; Kanan, M. W. CO_2 Reduction at Low Overpotential on Cu Electrodes Resulting from the Reduction of Thick Cu_2O Films. *J. Am. Chem. Soc.* **2012**, *134*, 7231−7234.
(43) Chen, Y.; Li, C. W.; Kanan, M. W. Aqueous CO_2 Reduction at Very Low Overpotential on Oxide-Derived Au Nanoparticles. *J. Am. Chem. Soc.* **2012**, *134*, 19969−19972.
(44) Rasul, S.; Anjum, D. H.; Jedidi, A.; Minenkov, Y.; Cavallo, L.; Takanabe, K. A Highly Selective Copper-Indium Bimetallic Electrocatalyst for the Electrochemical Reduction of Aqueous CO_2 to CO. *Angew. Chem., Int. Ed.* **2015**, *54*, 2146−2150.
(45) Lv, J. J.; Jouny, M.; Luc, W.; Zhu, W.; Zhu, J. J.; Jiao, F. A Highly Porous Copper Electrocatalyst for Carbon Dioxide Reduction. *Adv. Mater.* **2018**, *30*, 1803111.
(46) Gabardo, C. M.; Seifitokaldani, A.; Edwards, J. P.; Dinh, C. T.; Burdyny, T.; Kibria, M. G.; O'Brien, C. P.; Sargent, E. H.; Sinton, D. Combined High Alkalinity and Pressurization Enable Efficient CO_2 Electroreduction to CO. *Energy Environ. Sci.* **2018**, *11*, 2531−2539.
(47) Salvatore, D. A.; Weekes, D. M.; He, J.; Dettelbach, K. E.; Li, Y. C.; Mallouk, T. E.; Berlinguette, C. P. Electrolysis of Gaseous CO_2 to CO in a Flow Cell with a Bipolar Membrane. *ACS Energy Lett.* **2018**, *3*, 149−154.
(48) Lu, X.; Wu, Y.; Yuan, X.; Huang, L.; Wu, Z.; Xuan, J.; Wang, Y.; Wang, H. High-Performance Electrochemical CO_2 Reduction Cells Based on Non-Noble Metal Catalysts. *ACS Energy Lett.* **2018**, *3*, 2527−2532.
(49) Verma, S.; Hamasaki, Y.; Kim, C.; Huang, W.; Lu, S.; Jhong, H. R. M.; Gewirth, A. A.; Fujigaya, T.; Nakashima, N.; Kenis, P. J. A. Insights into the Low Overpotential Electroreduction of CO_2 to CO on a Supported Gold Catalyst in an Alkaline Flow Electrolyzer. *ACS Energy Lett.* **2018**, *3*, 193−198.

DOI: 10.1021/acscatal.8b05109
ACS Catal. 2019, 9, 3783−3791